

Low-temperature removal of toluene and propanal over highly active mesoporous CuCeO_x catalysts synthesized via a simple self-precipitation protocol

Chi He^{a,b}, Yanke Yu^a, Lin Yue^c, Nanli Qiao^c, Jinjun Li^d, Qun Shen^e, Weijia Yu^a, Jinsheng Chen^{a,**}, Zhengping Hao^{c,*}

^a Key Lab of Urban Environment and Health, Institute of Urban Environment, Chinese Academy of Sciences, Xiamen 361021, PR China

^b Department of Environmental Science and Engineering, School of Energy and Power Engineering, Xi'an Jiaotong University, Xi'an 710049, PR China

^c Department of Environmental Nano-materials, Research Center for Eco-Environmental Sciences, Chinese Academy of Sciences, Beijing 100085, PR China

^d School of Resource and Environmental Science, Hubei Key Laboratory of Biomass-Resources, Wuhan University, Wuhan 430079, PR China

^e Research Center for Greenhouse Gases and Environmental Engineering, Shanghai Advanced Research Institute, Chinese Academy of Sciences, Shanghai 201210, PR China

ARTICLE INFO

Article history:

Received 6 June 2013

Received in revised form 19 July 2013

Accepted 25 August 2013

Available online 31 August 2013

Keywords:

Self-precipitation

Mesoporous CuCeO_x

Catalytic oxidation

Toluene

Propanal

ABSTRACT

A series of CuCeO_x binary oxide catalysts with high specific surface area and mesoporous structure were synthesized by a facile self-precipitation approach. Toluene and propanal were adopted as the probe pollutants to evaluate their catalytic performance. The techniques such as XRD, N₂ adsorption/desorption, FE-SEM, TEM, H₂-TPR, XPS, Raman, DRUV-vis, and XANES, were employed for catalyst characterization. It is shown that plenty of Cu²⁺ ions in mesoporous CuCeO_x oxides are incorporated into CeO₂ lattice in the form of Cu_xCe_{1-x}O_{2-δ} solid solution, which produces large amounts of oxygen vacancies in the interface of CuO_x and CeO₂ oxides. Meanwhile, the Cu²⁺-O²⁻-Ce⁴⁺ connection in the solid solution can act as a bridge for oxygen transfer between Cu and Ce, and enhance the reducibility of both components. The activity of mesoporous CuCeO_x catalysts exhibits a volcano-type behavior with the increase of the Cu content, and the sample with Cu/Ce atomic ratio of 3/7 exhibits the highest catalytic efficiency. At GHSV of 36,000 h⁻¹, the temperatures for 90% toluene and propanal conversion over Cu_{0.3}Ce_{0.7}O_x sample are 212 and 192 °C, respectively, which are much lower than the catalysts synthesized via the incipient impregnation and thermal combustion methods. The co-combustion result demonstrates that propanal oxidation can be remarkably suppressed by the introduction of toluene due to the stronger surface affinity of toluene molecules. It can be concluded that both the higher surface oxygen adspecies concentration and better low-temperature reducibility were responsible for the superior activity of mesoporous CuCeO_x catalysts.

© 2013 Elsevier B.V. All rights reserved.

1. Introduction

Volatile organic compounds (VOCs) produced by human activities are an important class of air pollutants. Most of VOCs are precursors of ozone and photochemical smog, which are great threats to the environment and human health due to their toxic, carcinogenic, mutagenic, and teratogenetic nature [1]. Various strategies such as adsorption, absorption, pyrolysis, catalytic oxidation, and photocatalytic degradation have been developed for VOCs elimination. It is believed that the removal of VOCs by means of catalytic combustion is one of the most effective methods [2].

Nonetheless, the key issue for such an approach is still the availability of the economic and efficient catalyst.

In the past decades, supported noble metals or metal oxides, and mixed metal oxides have been explored and employed for VOCs elimination [3]. Although noble metal catalysts are catalytically more active at low temperature in comparison with the other metal oxides, the high cost, limited availability, and low resistance to halogens greatly restrict their large-scale application [4–6]. Among the transition metal oxides, the copper oxide loaded catalysts are known to be very active for VOCs combustion [7,8]. Cerium dioxide is widely used as a support for many oxidation catalysts due to its low temperature reducibility, high oxygen storage capacity, and electron release properties [9]. CuO-CeO₂ was found to be very powerful catalyst for oxidation reactions, which was even comparable to the supported noble metal catalysts [10–12] as the introduction of ceria can stabilize the active Cu sites, affect the Cu redox

* Corresponding author. Tel.: +86 10 62923564; fax: +86 10 62923564.

** Corresponding author. Tel.: +86 592 6190765; fax: +86 592 6190765.

E-mail addresses: jschen@iue.ac.cn (J. Chen), zpinghao@rcees.ac.cn (Z. Hao).

property, and improve the oxygen diffusivity and storage capacity of the composite catalyst [7,13]. It is well-known that preparation method can greatly influence the properties of the target catalysts. Different protocols such as incipient impregnation, urea-nitrate combustion, sol-gel, and coprecipitation have been studied for the synthesis of highly efficient transition metal oxides loaded catalysts, while the surface areas of the obtained catalysts were rather low [6,14,15]. Recently, a new method involving a surfactant in the precipitation process was reported, and the obtained catalysts show relatively high specific surface areas and improved catalytic performance. Various mesoporous metal oxides (Mn_2O_3 , Fe_2O_3 , CuO , etc.) have been synthesized by Liu et al. with cetyltrimethylammonium bromide (CTAB) or polyethylene glycol (PEG) as the template [16]. Cao et al. have also synthesized CuO - Fe_2O_3 and CuO - $Ce_{0.8}Zr_{0.2}O_2$ catalysts with large surface areas and worm-like mesoporous structures by using the CTAB template [17,18]. High surface area CuO - CeO_2 catalysts were prepared using CTAB as the soft template and sodium hydroxide as the precipitating agent, and this material shows high catalytic activity for CO oxidation [11].

In our previous work, mesoporous metal oxides such as Au/Co_3O_4 - CeO_2 , Co_3O_4 - CeO_2 , and Au/Co_3O_4 have been developed by using SBA-15 or KIT-6 as the hard template, and these materials showed good activities for formaldehyde and ethylene elimination [19,20]. Herein, we report a low cost and universal self-precipitation (SP) method that can be adopted to facilely synthesize mesoporous metal oxides. Toluene and propanal are two types of typical aromatic and oxygen-contained hydrocarbons vast existed in industrial processes, which make enormous threats to the environment and human health. Herein, toluene and propanal were adopted as the probe pollutants to evaluate the removal effectiveness of the mesostructured $CuCeO_x$ materials. The experimental results show that highly crystalline foamlke mesoporous metal oxide with very high surface area and narrow pore size distribution can be obtained. The mesopores $CuCeO_x$ oxides possess much higher toluene and propanal low-temperature catalytic activities than their counterparts synthesized by the incipient impregnation and thermal combustion methods. The catalytic performance of the all prepared catalysts is well correlated with their physicochemical parameters (*i.e.*, surface area, reducibility, and surface oxygen concentration), and the potential reaction scheme for toluene and propanal oxidation involving interface oxygen vacancy and oxygen adspecies is proposed.

2. Experimental

2.1. Catalyst preparation

All chemicals used in the synthesis route are cheap metal salts, CTAB, urea, and water. The related catalysts with different $Cu/(Cu + Ce)$ atomic ratios, denoted as $Cu_aCe_{1-a}O_x$ ($a = 0.15$, 0.3 , and 0.4), were prepared by the self-precipitation approach. Typically, different amounts of $Cu(NO_3)_2 \cdot 3H_2O$, $Ce(NO_3)_3 \cdot 6H_2O$, 4.4 g of CTAB, and 6 g of urea were dissolved in 150 mL of H_2O ($n_{CTAB}:n_{Ce} = 1:1$). After stirring for 2 h , the solutions were aged in autoclaves at 80°C for 24 h , and followed by 12 h at 120°C . Then, the products were washed with distilled water and recovered by centrifugation. Finally, the recovered products were dried at 80°C and calcined at 550°C for 4 h to remove organic residues.

For comparison, the $CuCeO_x$ oxides with Cu loading of 30 at\% were prepared by the incipient impregnation (imp) and thermal combustion (tcb) methods, and denoted as $CuCeO_x$ -imp and $CuCeO_x$ -tcb, respectively [15,21]. In addition, pure CuO and CeO_2 were also synthesized through thermal calcination their corresponding hydrated metal nitrates at 550°C for 4 h .

2.2. Catalyst characterizations

X-ray diffraction (XRD) patterns were recorded on a Philips X'Pert powder diffraction system using $Cu K\alpha$ radiation ($\lambda = 0.15418\text{ nm}$) in the 2θ range of $0.7\text{--}5^\circ$ (scanning rate of $0.5^\circ/\text{min}$) and $10\text{--}80^\circ$ (scanning rate of $4^\circ/\text{min}$), respectively. N_2 adsorption/desorption isotherms of catalysts at 77 K were collected on a Quantachrome NOVA 1200e gas sorption analyzer. All samples were degassed under vacuum at 300°C for 3 h before the measurement. The total pore volume was estimated from the amount of nitrogen adsorbed at a relative pressure (P/P_0) of *ca.* 0.99 . The specific surface area was calculated using the Brunauer–Emmett–Teller (BET) method, and the pore size distribution was derived from the desorption branch of the N_2 isotherm using the Barrett–Joyner–Halenda (BJH) method. Field emission scanning electron microscopy (FE-SEM) images were recorded on a Hitachi S-4800 microscope. Transmission electron microscopy (TEM) images were collected on a Hitachi H-7650 microscope operating at an acceleration voltage of 80 kV . The actual Cu content was determined by inductively coupled plasma optical emission spectroscopy (ICP-OES) on a PerkinElmer OPTIMA 7000 DV, and the result shows that the Cu loading in the final catalyst is approximately equal to the theoretical value. Temperature programmed reduction (H_2 -TPR) experiments were performed on a Quantachrome ChemBET 3000 TPR-TPD analyzer. Prior to reduction, 50 mg of the catalyst was heated in a $5\% O_2/He$ flow ($50\text{ mL}/\text{min}$) from room temperature to 500°C and held for 30 min , and then treated in a He stream at room temperature for 30 min to remove any residual oxygen. The sample was finally reduced under a $5\% H_2/He$ ($50\text{ mL}/\text{min}$) from 50 to 700°C with a heating rate of $10^\circ\text{C}/\text{min}$. X-ray photoelectron spectroscopy (XPS) experiments were carried out on a Quantum 2000 instrument under high vacuum ($<5 \times 10^{-10}\text{ Torr}$) using $Al K\alpha$ as the exciting radiation at a constant pass energy of 1486.6 eV . The C 1s peak was used to calibrate the binding energy. X-ray absorption fine structure (XAFS) data of $Cu_{0.3}Ce_{0.7}O_x$ were measured on 4W1B beamline at the Beijing Synchrotron Radiation Facility (BSRF). A spectral range of $8.820\text{--}9.640\text{ keV}$ from the K-absorption edge of 8.990 keV was collected under ambient conditions. Si (1 1 1) monochromator crystal was used and the XAFS spectra of adsorption samples were collected with a Lytle ionization detector in fluorescence mode. An average of three scans was performed to achieve an adequate signal/noise ratio, and the energy of Cu K-absorption edge was calibrated with Cu foil. The XAFS data were processed following the standard procedure of background absorption removal and normalization. Raman spectra were obtained on a Horiba Jobin Yvon S.A.S. LabRAM Aramis spectrometer at ambient temperature and moisture-free conditions. The emission line at 532 nm from an Ar^+ ion laser was focused, analyzing spot about 1 mm . Time of acquisition was varied according to the intensity of the Raman scattering, and the wave numbers obtained from spectra were accurate to within 1 cm^{-1} .

2.3. Catalytic activity

All evaluation experiments were performed in a continuous-flow fixed-bed reactor at the atmospheric pressure, consisting of a stainless steel tube (6 mm i.d.) that was filled with the catalyst. In combustion experiments, the saturators contained toluene and propanal solutions were heated and maintained at 80°C , and the VOC-containing streams were produced by bubbling air through the VOC saturators, and then the single/mixture VOC-containing gas were further diluted with another air stream to reach the required concentration before reaching the reaction bed. The temperatures of the catalyst bed and tubular electric furnace were monitored automatically by E-type thermocouples. In each test,

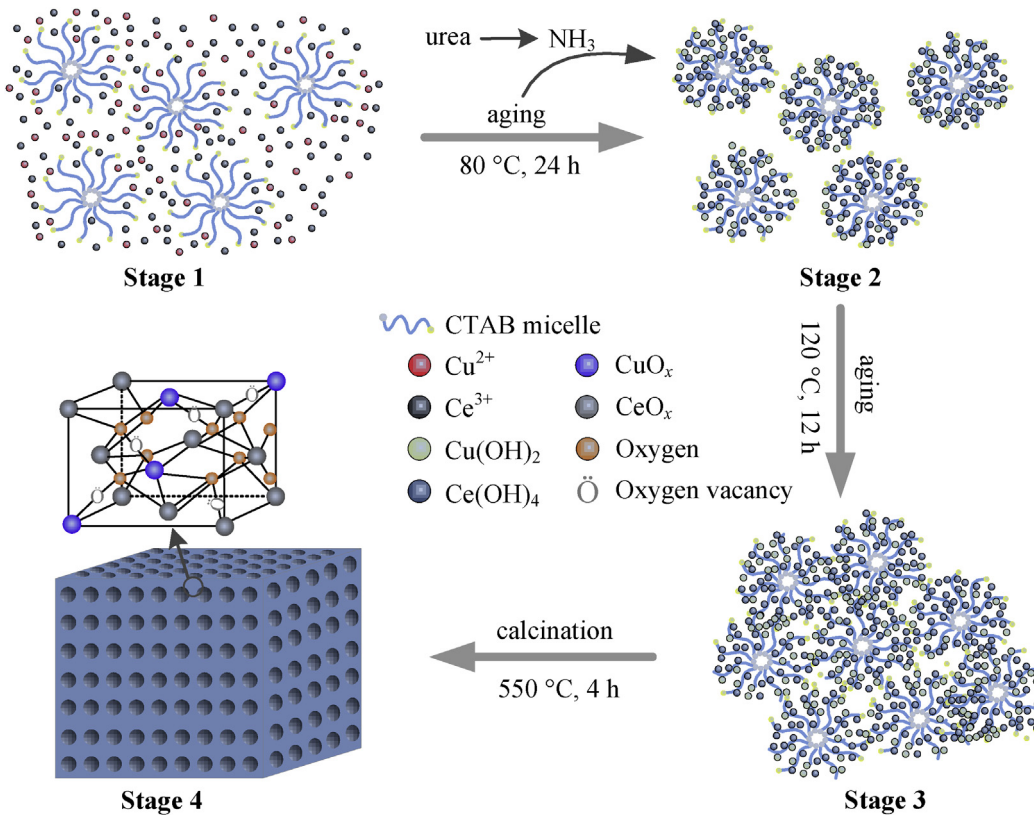


Fig. 1. Schematic illustration of the formation mechanism for the mesoporous CuCeO_x oxides.

300 mg of the catalyst (40–60 mesh) was placed at the middle of the tube reactor and the total flow rate was kept at 350 mL/min, i.e., gas hourly space velocity (GHSV) of ca. 36,000 h^{-1} , and the O_2 feed concentration was kept at about 21% (v/v). In each test, the catalyst bed temperature was first raised to 120 °C with the feed stream passing and stabilized for 30 min. Then the temperature was increased to the next one at a heating rate of 5 °C/min and stabilized for 20 min prior to online analysis of the effluent gas composition in a gas chromatograph (GC9890A, Shanghai Linghua Co., China) equipped with the flame ionization detector (FID). The reaction byproducts were identified by the FID and a Hiden QGA on-line mass spectrometer.

3. Results and discussion

3.1. Formation of mesoporous CuCeO_x metal oxides

The mesoporous CuCeO_x catalysts were synthesized through a simple self-deposition process, as displayed in Fig. 1. The metal ions, urea molecules, CTAB micelles are firstly random dissolved in water, and all components are homogeneous dispersed in the mixed solution after 2 h stirring (stage 1). Urea is believed to play an indispensable role in the formation of mesoporous metal oxides [22]. When the mixture is heated to 80 °C, urea starts to decompose and slowly releases ammonia into the aqueous solution, and OH^- anions are gradually formed. Steady supply of the OH^- anions causes a persistent precipitation of corresponding metal hydroxides, which grow around the CTAB/water micelles (stage 2). The polycondensation and rearrangement process of CTAB/water micelles will happen when CTAB micelles aged at 120 °C (stage 3), and the crystallized mesoporous metal oxides will be finally obtained after removing the CTAB organic residues at 550 °C in air (stage 4).

3.2. Crystal structure and textural property

Fig. 2 shows the wide-angle XRD patterns of various catalysts. The main reflections at $2\theta = 28.5^\circ, 33.0^\circ, 47.5^\circ, 56.3^\circ, 59.2^\circ, 69.3^\circ$,

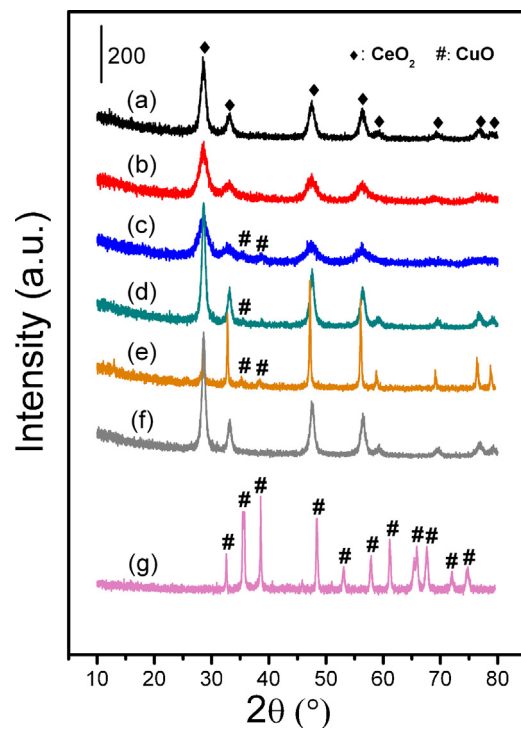


Fig. 2. XRD patterns of (a) $\text{Cu}_{0.15}\text{Ce}_{0.85}\text{O}_x$, (b) $\text{Cu}_{0.3}\text{Ce}_{0.7}\text{O}_x$, (c) $\text{Cu}_{0.4}\text{Ce}_{0.6}\text{O}_x$, (d) CuCeO_x -imp, (e) CuCeO_x -tcb, (f) CeO_2 , and (g) CuO .

Table 1Summary of the XRD, N₂ sorption, and XPS results.

Sample	d_{111} (Å)	C _d ^a (nm)	M _s ^b	S _{BET} ^c (m ² /g)	D _v ^d (cm ³ /g)	D _p ^e (nm)	Cu ^f (at%)	Ce ^{3+g} (%)	O _{sur} ^h (%)
Cu _{0.15} Ce _{0.85} O _x	5.4214	14.6	0.0092	117.2	0.15	2.8	9.7	34.6	36.4
Cu _{0.3} Ce _{0.7} O _x	5.4169	8.9	0.0158	162.8	0.17	2.5	21.2	36.2	40.6
Cu _{0.4} Ce _{0.6} O _x	5.4130	6.3	0.0184	139.5	0.17	2.7	36.3	37.5	34.7
CuCeO _x -imp	5.4148	15.7	0.0088	59.1	0.16	5.5	37.1	31.2	31.5
CuCeO _x -tcb	5.4125	64.1	0.0022	3.9	0.01	5.3	42.6	23.3	25.3
CuO	/	/	/	0.1	/	5.4	/	/	/
CeO ₂	5.4276	16	0.0087	60.8	0.18	6.1	/	/	/

Note: ^aCrystallite size and ^blattice microstrain calculated by the Scherrer equation from the (1 1 1) reflection of CeO₂; ^cBET specific surface area calculated at P/P₀ = 0.05–0.25;^dTotal pore volume estimated at P/P₀ = 0.99; ^eBJH pore diameter calculated from the desorption branch; ^fThe Cu content estimated by XPS analysis; ^gThe Ce³⁺ ratio obtained from the Ce 3d result; ^hPercentage of the surface oxygen species over various catalysts.

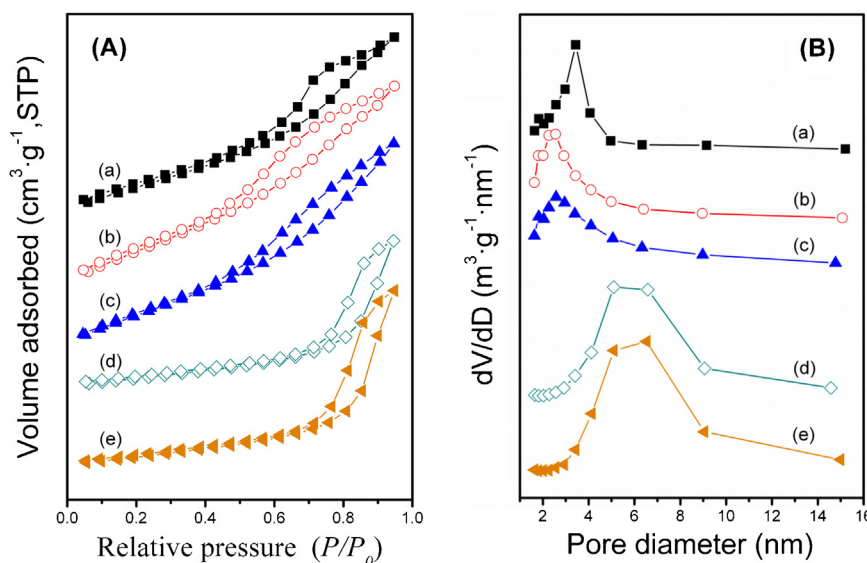
and 76.7° over all CuCeO_x catalysts are indexed well to the typical cubic fluorite-like structure of CeO₂ (JCPDS No. 81-0792). It can be seen that no diffraction peaks corresponding to CuO or Cu₂O (JCPDS No. 80-1268) can be found when the copper loading below 30 at%, which may be due to the high dispersion of Cu nanoparticles with too small particle sizes on the surface of ceria support to be identified by the XRD or the localization of Cu ions in the CeO₂ lattice [23]. The weak diffraction peaks attributed to CuO crystal phase appear at 2θ = 35.2° and 38.3° in Cu_{0.4}Ce_{0.6}O_x, CuCeO_x-imp, and CuCeO_x-cop samples, suggesting the partial aggregation of Cu phase. Table 1 lists the lattice parameter and lattice microstrain of the synthesized catalysts. The slight decrease of the CeO₂ lattice parameter (5.4276 Å) after the introduction of copper species (5.4125–5.4214 Å) provides the evidence that part of Cu ions are incorporated into the CeO₂ crystallites, by considering that the radius of Cu⁺ ions (0.96 Å) or Cu²⁺ ions (0.73 nm Å) is smaller than that of Ce³⁺ (1.10 Å) or Ce⁴⁺ ions (1.01 Å). In addition, the higher lattice microstrain value of CuCeO_x oxides also proves the incorporation of Cu species.

The N₂ adsorption/desorption isotherms and pore size distribution of CuCeO_x oxides and CeO₂ support are shown in Fig. 3. All Cu_aCe_{1-a}O_x samples exhibit typical IV shape isotherms with the P/P₀ of the inflection point corresponding to a diameter in the mesoporous range [24], which are much different from those of CuCeO_x-imp and pure CeO₂ (Fig. 3A). The BJH pore size distribution curves of Cu_aCe_{1-a}O_x exhibit one single narrow peak centered at ca. 1.5–4.0 nm (Fig. 3B), suggesting the good homogeneity of the mesopores. Table 1 displays the specific surface area (S_{BET})

total pore volume (D_v), and mean pore diameter (D_p) of various samples. All the three Cu_aCe_{1-a}O_x samples, including that with atomic ratio of Cu/(Cu + Ce) as high as 40%, show large S_{BET} exceeding 110 m²/g, indicating the effectiveness of the SP method for the synthesis of metal oxides possessing high specific surface area. The S_{BET} of Cu_aCe_{1-a}O_x catalysts reach the maximum value when the Cu/(Cu + Ce) equal to 30 at% (162.8 m²/g), while the S_{BET} value decreases to some extent either reduce or enhance the Cu content. In general, the S_{BET} of all Cu_aCe_{1-a}O_x catalysts (117.2–162.8 m²/g) are much higher than the samples synthesized via other approaches (0.1–60.8 m²/g), while the D_p of Cu_aCe_{1-a}O_x samples (2.5–2.8 nm) are a little lower than those of the CuCeO_x-imp (5.5 nm), CuCeO_x-tcb (5.3 nm), and CeO₂ support (6.1 nm).

3.3. Morphology and reducibility

The morphological properties of representative catalysts are investigated by FE-SEM, as shown in Fig. 4. Cu_{0.3}Ce_{0.7}O_x and CuCeO_x-imp catalysts possess shaggy surfaces with a large degree of porosity, while the metal nanoparticles over CuCeO_x-imp sample accumulate to some extent (Fig. 4a and b). CuCeO_x-tcb shows a relatively smooth surface, and the metal particles over which are seriously aggregated (Fig. 4c), in well consistent with the XRD result (Fig. 2). Information about the microstructure of the CuCeO_x mixed oxides is further studied by TEM, as displayed in Fig. 4. No well-defined mesoporous structure, like those in Si-based molecules sieves, could be found in all Cu_aCe_{1-a}O_x catalysts, suggesting that these mesopores are randomly distributed

**Fig. 3.** N₂ adsorption/desorption isotherms (A) and pore size distribution (B) of (a) Cu_{0.15}Ce_{0.85}O_x, (b) Cu_{0.3}Ce_{0.7}O_x, (c) Cu_{0.4}Ce_{0.6}O_x, (d) CuCeO_x-imp, and (e) CeO₂.

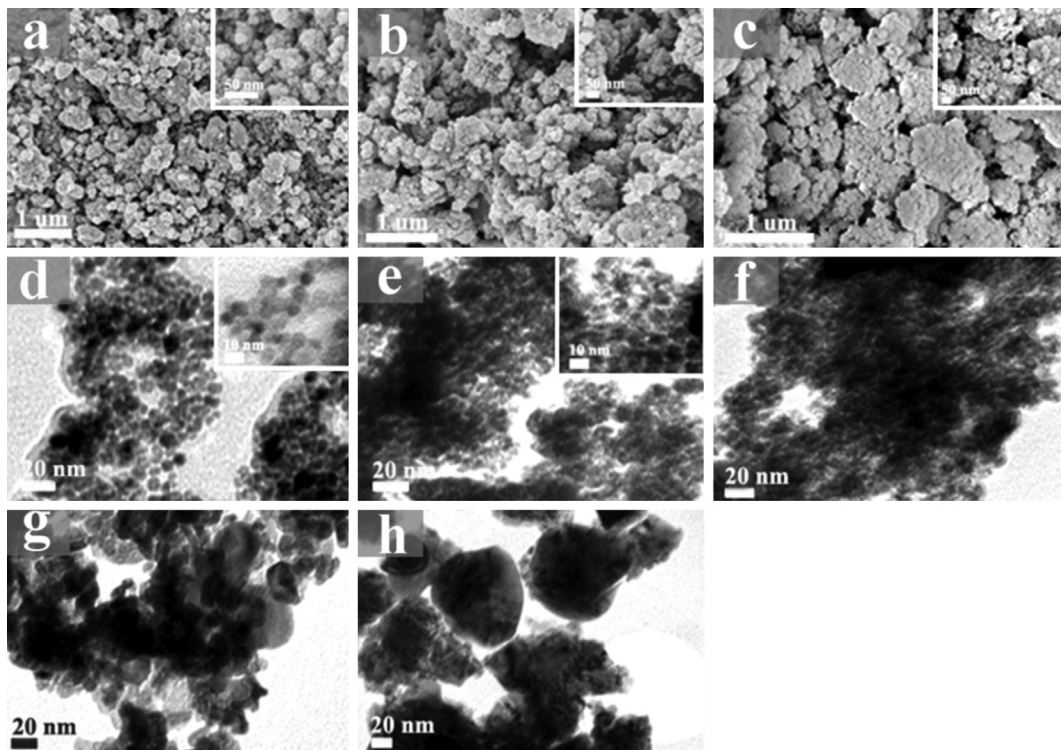


Fig. 4. Representative SEM (a–c) and TEM (d–h) images of various catalysts: (a) $\text{Cu}_{0.3}\text{Ce}_{0.7}\text{O}_x$, (b) $\text{Cu}\text{Ce}\text{O}_x\text{-imp}$, (c) $\text{Cu}\text{Ce}\text{O}_x\text{-tcb}$, (d) $\text{Cu}_{0.15}\text{Ce}_{0.85}\text{O}_x$, (e) $\text{Cu}_{0.3}\text{Ce}_{0.7}\text{O}_x$, (f) $\text{Cu}_{0.4}\text{Ce}_{0.6}\text{O}_x$, (g) $\text{Cu}\text{Ce}\text{O}_x\text{-imp}$, and (h) $\text{Cu}\text{Ce}\text{O}_x\text{-tcb}$.

among a mixture of small nanoparticles. A little portion of particles are agglomerated over the $\text{Cu}_{0.3}\text{Ce}_{0.7}\text{O}_x$ catalyst, and this phenomenon is more obvious when further increase the Cu content (Fig. 4d–f). As for the $\text{Cu}\text{Ce}\text{O}_x\text{-imp}$ and $\text{Cu}\text{Ce}\text{O}_x\text{-tcb}$ samples, the metal precursors are prone to agglomerated into cluster with calculated diameter higher than 40 and 200 nm, respectively (Fig. 4g and h).

The reducibility of the mixed oxide catalysts as well as the corresponding individual components is investigated by $\text{H}_2\text{-TPR}$, as displayed in Fig. 5. Pure CuO shows a single reduction peak (β) of maximum hydrogen consumption at about 373°C , while CeO_2 shows two weak reduction peaks centered at around 415 and 517°C (γ_1 and γ_2), attributing to the reduction of surface oxygen and bulk oxygen, respectively [25]. A different reduction profiles are observed for the mesoporous $\text{Cu}_x\text{Ce}_{1-x}\text{O}_x$ catalysts. $\text{Cu}_{0.3}\text{Ce}_{0.7}\text{O}_x$ and $\text{Cu}_{0.4}\text{Ce}_{0.6}\text{O}_x$ possess three overlapping reduction peaks (α , β_1 and β_2) in the temperature range of $90\text{--}225^\circ\text{C}$, which is much lower than that of pure CuO . It has been reported that CeO_2 promotes the reduction of finely dispersed CuO surface species, and the smaller the CuO particles, the easier they are to reduce [26,27]. Bulk CuO is reducible at higher temperatures, and has a small contribution to catalytic activity. The reduction peaks around at 100 and 170°C (α and β_1) are respectively attributed to the reduction of well dispersed Cu species and Cu ions strongly interacting with CeO_2 [25], and reduction peaks at $200\text{--}300^\circ\text{C}$ correspond to the contribution of crystalline CuO [7]. The signal peaks (γ_1) exceed 300°C probably associated with the reduction of CeO_2 . $\text{Cu}\text{Ce}\text{O}_x\text{-imp}$ sample is easier reduced than the $\text{Cu}\text{Ce}\text{O}_x\text{-tcb}$ catalyst (β_3) due to the better dispersion of copper species, in accordance with the XRD and TEM results (Figs. 2 and 3). Compared with CuO and CeO_2 , the reduction peaks of the mixed oxides systematically shift to the lower temperature side, suggesting that the reducibility is promoted by the interaction of CuO and CeO_2 , probably in the form of $\text{Cu}_x\text{Ce}_{1-x}\text{O}_{2-\delta}$ solid solution. The $\text{Cu}^{2+}\text{-O}^{2-}\text{-Ce}^{4+}$ connection in $\text{Cu}_x\text{Ce}_{1-x}\text{O}_{2-\delta}$ solid solution could reduce the redox potential of Cu species as well as

act as a bridge for O transfer between Cu and Ce. Thus, the interaction between Cu and Ce in the solid solution assures enhanced reducibility for both compounds, and this allows having an effective redox cycle during oxidation reactions.

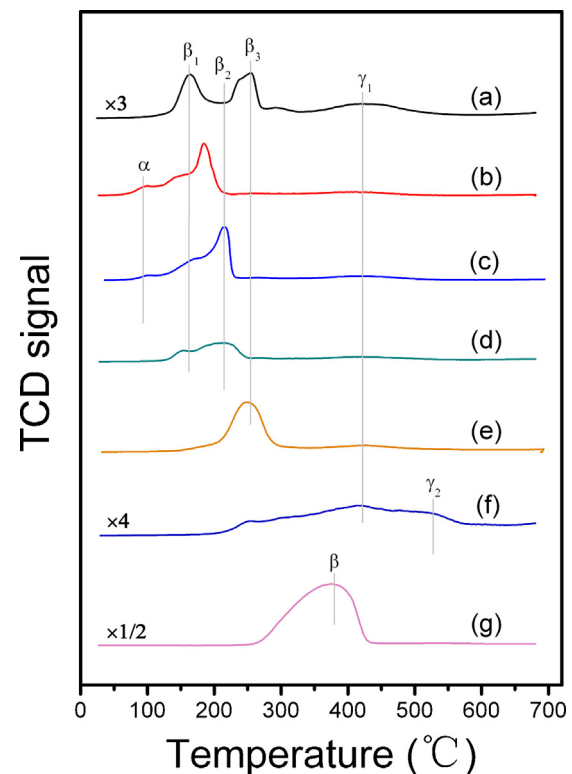


Fig. 5. $\text{H}_2\text{-TPR}$ profiles of (a) $\text{Cu}_{0.15}\text{Ce}_{0.85}\text{O}_x$, (b) $\text{Cu}_{0.3}\text{Ce}_{0.7}\text{O}_x$, (c) $\text{Cu}_{0.4}\text{Ce}_{0.6}\text{O}_x$, (d) $\text{Cu}\text{Ce}\text{O}_x\text{-imp}$, (e) $\text{Cu}\text{Ce}\text{O}_x\text{-tcb}$, (f) CeO_2 , and (g) CuO .

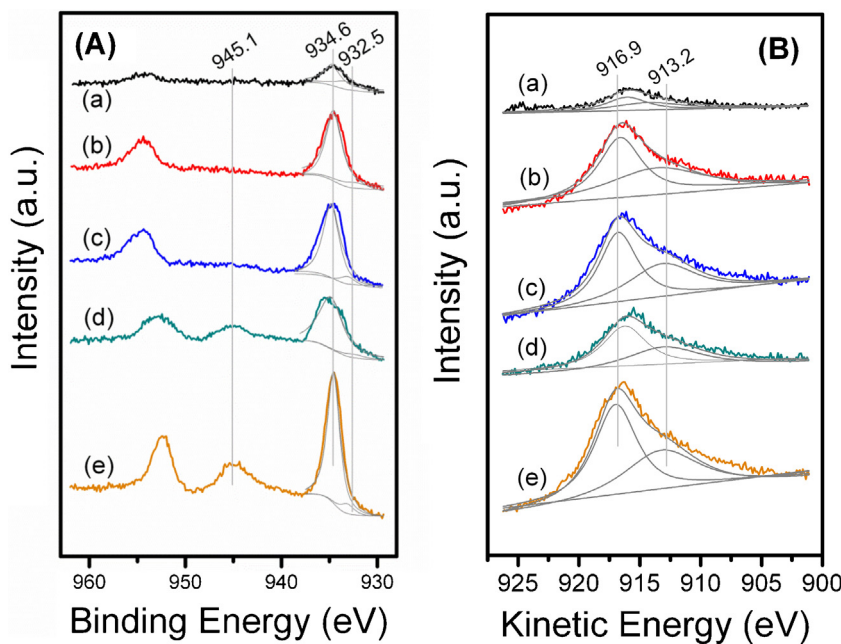


Fig. 6. Cu 2p and Cu LMM Auger kinetic energy spectra of (a) $\text{Cu}_{0.15}\text{Ce}_{0.85}\text{O}_x$, (b) $\text{Cu}_{0.3}\text{Ce}_{0.7}\text{O}_x$, (c) $\text{Cu}_{0.4}\text{Ce}_{0.6}\text{O}_x$, (d) $\text{CuCeO}_x\text{-imp}$, and (e) $\text{CuCeO}_x\text{-tcb}$.

3.4. Surface state and structure characteristic

The information of surface composition and chemical state of the synthesized catalysts was studied by XPS. The surface composition, represented as the $[\text{Cu}/(\text{Cu} + \text{Ce})] \times 100\%$ (atomic ratio), is displayed in Table 1. It can be observed that the surface contents of Cu species in all $\text{Cu}_a\text{Ce}_{1-a}\text{O}_x$ catalysts are a little lower than the theoretical values, indicating that Cu ions are highly dispersed over the support or into the CeO_2 lattice, possibly in the form of $\text{Cu}_x\text{Ce}_{1-x}\text{O}_{2-\delta}$ solid solution. The incipient impregnation and thermal combustion methods used for catalyst preparation result in the surface Cu enrichment, and probably induces Cu species aggregation in bulk. The presence of CuO peaks in XRD diffraction patterns of $\text{CuCeO}_x\text{-imp}$ and $\text{CuCeO}_x\text{-tcb}$ also confirms this inference (Fig. 2). Fig. 6A shows the Cu 2p binding energy of various samples. The principal peak at binding energy of 934.5 eV over CuCeO_x catalysts indicates the presence of Cu^{2+} , and the weak shake-up peak at 940–948 eV and the peak at binding energy of 932.5 eV suggest the existence of reduced copper species [21]. As is known, the Cu 2p_{3/2} binding energy cannot distinguish the Cu^+ and Cu^0 as they are essentially identical. Thus, the Cu LMM Auger lines were further investigated, as shown in Fig. 6B. The board feature of the Cu LMM Auger kinetic energy spectra consists of the contribution of two kinds of Cu species. The peaks in the Auger kinetic spectra of 916.9 and 913.2 eV should respectively correspond to the Cu^{2+} and Cu^{1+} species as there are no literature data for metallic copper with such low Auger kinetic energy. Similarity, the coexistence of Cu^{1+} and Cu^{2+} ions in CuO-CeO_2 catalysts also has been found by other researchers [28,29]. Hočevá et al. [30] proposed that the formation of Cu^{1+} might be induced by substitution of Cu^{1+} and Ce^{4+} at the interface of two oxide phases. Likewise, the DRUV-vis absorption peak at around 451 nm also proves the presence of Cu^{1+} in the synthesis catalysts (see Fig. S1) [31]. The experimental and fitted Ce 3d spectra of the synthesized catalysts are shown in Fig. 7, and the fitting process was referred to the literature [32]. The Ce^{3+} relative content (see Table 1) can be determined by $\text{Ce}^{3+}/(\text{Ce}^{3+} + \text{Ce}^{4+}) \times 100\%$, where $\text{Ce}^{3+} = (u' + u_0 + v' + v_0)$ and $\text{Ce}^{4+} = (u'' + u'' + u + v'' + v'' + v + v_0)$. The results in Table 1 reveal that there is no significant difference for the Ce^{3+} percentages among mesoporous $\text{Cu}_a\text{Ce}_{1-a}\text{O}_x$ samples with different Cu/Ce ratios. It is

reported that the existence of Ce^{3+} in CeO_2 implies the formation of an oxygen vacancy [33]. Therefore, it can be inferred that the oxygen vacancies are always present in $\text{Cu}_a\text{Ce}_{1-a}\text{O}_x$ oxides. In addition, the Ce^{3+} contents in $\text{Cu}_a\text{Ce}_{1-a}\text{O}_x$ catalysts are higher than those of $\text{CuCeO}_x\text{-imp}$ and $\text{CuCeO}_x\text{-tcb}$ samples, suggesting that the SP method can create more oxygen vacancies than the incipient impregnation and thermal combustion approaches. The O 1s XPS spectrum of pure CeO_2 can be divided into four peaks with the core level of lattice oxygen at 528.9 eV [9]. Herein, the O 1s XPS spectra of the synthesized catalysts can be resolved into three peaks by deconvolution, as can be seen in Fig. 8. The binding energy at ca. 529.4 eV assigned to the lattice oxygen (O_{latt}). Two shoulder peaks ca. 531.3 (O_{sur} : active oxygen) and 532.7 (O_{ads}) eV can be attributed to the adsorbed oxygen and weakly bonded oxygen species, and to the adsorbed oxygen from the hydroxyl species and adsorbed water species as contaminant on the surface, respectively [4]. Comparing with CeO_2 , the O 1s core level of O_{latt} over CuCeO_x samples shifts to higher values due to “O → Cu” electron-transfer processes, which can create active oxygen species such as O^\bullet , O_2^- , $\text{O}_2^{\cdot-}$, and

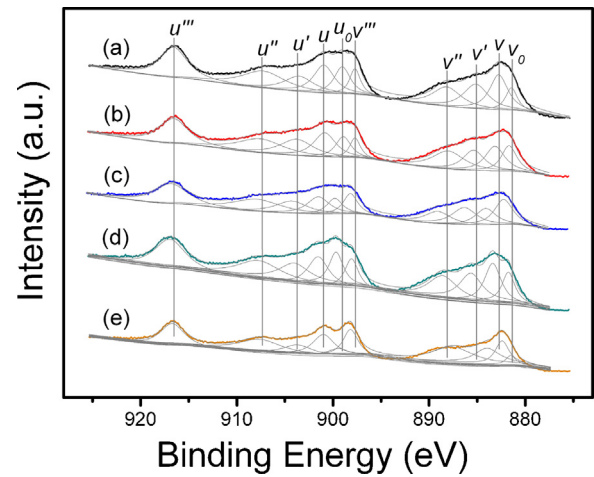


Fig. 7. Ce 3d XPS spectra (a) $\text{Cu}_{0.15}\text{Ce}_{0.85}\text{O}_x$, (b) $\text{Cu}_{0.3}\text{Ce}_{0.7}\text{O}_x$, (c) $\text{Cu}_{0.4}\text{Ce}_{0.6}\text{O}_x$, (d) $\text{CuCeO}_x\text{-imp}$, and (e) $\text{CuCeO}_x\text{-tcb}$.

Table 2

Catalytic performance of the synthesized catalysts.

Sample	T_{50}^a (°C)	T_{90}^a (°C)	T_{50}^b (°C)	T_{90}^b (°C)	r_1^c (mmol/g h)	r_2^d (mmol/g h)	E_{a1}^e (kJ/mol)	E_{a2}^f (kJ/mol)
Cu _{0.15} Ce _{0.85} O _x	198	231	204	250	0.87	2.25	108.8	114.4
Cu _{0.3} Ce _{0.7} O _x	187	212	172	192	1.29	4.14	105.4	90.5
Cu _{0.4} Ce _{0.6} O _x	223	268	227	263	0.49	1.16	120.5	141.7
CuCeO _x -imp	249	320	242	294	0.23	0.46	137.3	155
CuCeO _x -tcb	293	/	283	348	0.14	0.04	157.1	264.2
CuO	369	/	305	/	0.06	0.10	214.4	363.1
CeO ₂	/	/	/	/	0.04	/	162.1	499.4

Note: Temperatures at which 50% and 90% conversion of toluene^a and propanal^b; ^cToluene conversion rate gained at 220 °C; ^dPropanal conversion rate gained at 210 °C; ^eApparent activation energy for toluene^e and propanal^f combustion obtained from Arrhenius plot.

O-. Table 2 lists the active O_{sur} percentages of various catalysts. The Cu_{0.3}Ce_{0.7}O_x possesses the largest amount of O_{sur} (40.6%), which is much higher than that of CuCeO_x-imp (31.5%) and CuCeO_x-tcb (25.3%).

The edge energies and shapes of Cu_{0.3}Ce_{0.7}O_x and copper standard materials (*i.e.*, CuO, Cu₂O, and Cu foil) can provide important information about the oxidation state and local structure of Cu species (see Fig. 9). The peak centered at *ca.* 8.981 and 8.985 keV can respectively be attributed to the dipole-allowed 1s → 4p electron transition in Cu⁺ and Cu²⁺, and the weak pre-edge peak at 8.976 keV is ascribed to the dipole-forbidden electronic transition of 1s → 3d in Cu²⁺ [34]. Therefore, the weak edge transition peak centered at about 8.981 keV suggests the presence of Cu⁺ in

Cu_{0.3}Ce_{0.7}O_x sample, in accordance with the XPS and DRUV-vis results (Figs. 6 and S1). The absence of the edge transition peak at 8.978 and 8.982–8.987 keV, and the higher white line intensity between 8.992 and 9.007 keV in Cu_{0.3}Ce_{0.7}O_x can be ascribed to strong interaction of Cu and Ce species [35]. As is known, Cu ions incorporated into the ceria lattice can lead to the defective sites and oxygen vacancies (Ö) in the structure (*i.e.*, xCuO + (1 - x)CeO₂ → xCu_{—Ce²⁺} + xÖ + (2 - x)O²⁻ + (1 - x)Ce_{—Ce⁴⁺}). The oxygen vacancy quantity and distribution in Cu_aCe_{1-a}O_x oxides were investigated by Raman spectroscopy, as displayed in Fig. 10. The Raman spectra of CuO (three peaks at 295, 340, and 626 cm⁻¹) can be found elsewhere [36]. Pure CeO₂ support with fluorite-type structure has one sharp Raman peak at *ca.* 457 cm⁻¹ (Fig. 10A), while the corresponding Raman peaks over Cu_aCe_{1-a}O_x samples are shifted to lower frequencies (*ca.* 440 cm⁻¹) due to the formation of oxygen vacancies in CeO₂ lattice [37]. Moreover, the amount of oxygen vacancy over various catalysts (see Fig. 10B) was further calculated by Gaussian deconvolution the region around 595 cm⁻¹ [38]. It can be observed that the Cu_{0.3}Ce_{0.7}O_x catalyst possesses highest oxygen vacancy concentration (about twenty times higher than that of CeO₂), and the oxygen vacancy amount over Cu_{0.4}Ce_{0.6}O_x is close to that of Cu_{0.15}Ce_{0.85}O_x sample.

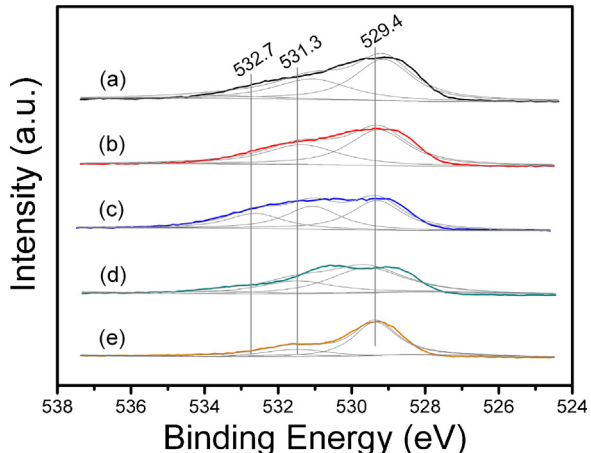


Fig. 8. O 1s XPS spectra of (a) Cu_{0.15}Ce_{0.85}O_x, (b) Cu_{0.3}Ce_{0.7}O_x, (c) Cu_{0.4}Ce_{0.6}O_x, (d) CuCeO_x-imp, and (e) CuCeO_x-tcb.

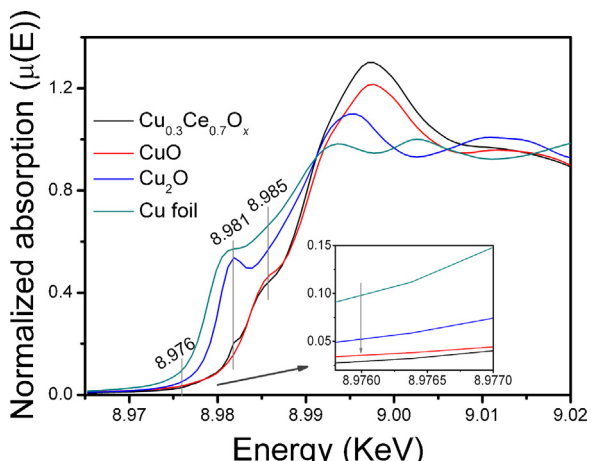


Fig. 9. Copper K-edge XANES spectra of Cu_{0.3}Ce_{0.7}O_x, CuO, Cu₂O, and Cu foil.

3.5. Catalytic removal of toluene and propanal

The catalytic behaviors of toluene and propanal oxidation in single and binary pollutant system were studied, as shown in Figs. 11–13. In addition, the specific reaction data (reaction temperature, reaction rate, and apparent activation energy) of all synthesized catalysts were also calculated and listed in Table 2. Above all, the blank tests were carried out with crushed quartz sand (40–60 mesh) packed in the reactor in order to check whether or not some reactions under thermal combustion condition could take place, and the results reveal that no thermal or homogeneous toluene and propanal destruction can be observed below 350 °C. All mesoporous Cu_aCe_{1-a}O_x oxides possess much higher low-temperature activity than those synthesized via the incipient impregnation and thermal combustion methods (Fig. 11). Cu_{0.3}Ce_{0.7}O_x has the best toluene catalytic activity ($T_{90} = 209$ °C), which is much higher than that of the CuCeO_x-imp ($T_{90} = 320$ °C) and CuCeO_x-tcb ($T_{90} > 400$ °C) catalysts (Table 2). The catalytic activity order of all samples is as follows: Cu_{0.3}Ce_{0.7}O_x > Cu_{0.15}Ce_{0.85}O_x > Cu_{0.4}Ce_{0.6}O_x > CuCeO_x-imp ≫ CuCeO_x-tcb ≫ CuO > CeO₂. The catalytic activity of Cu_{0.3}Ce_{0.7}O_x is extensively compared with the other representative catalysts used for toluene oxidation in the literature [3,6,10,39–49] considering it is conspicuous activity, as displayed in Table 3. It can be seen that the T_{90} temperatures for toluene conversion over most catalysts (either transition metals supported or noble metals-based samples) are much higher than that of the Cu_{0.3}Ce_{0.7}O_x catalyst. For instance, the T_{90} temperatures of 0.5%Pd/MAC ($T_{90} = 370$ °C) [40], 0.3%Pd/ZSM-5 ($T_{90} = 270$ °C) [41], Ag-Mn/SBA-15 ($T_{90} = 255$ °C)

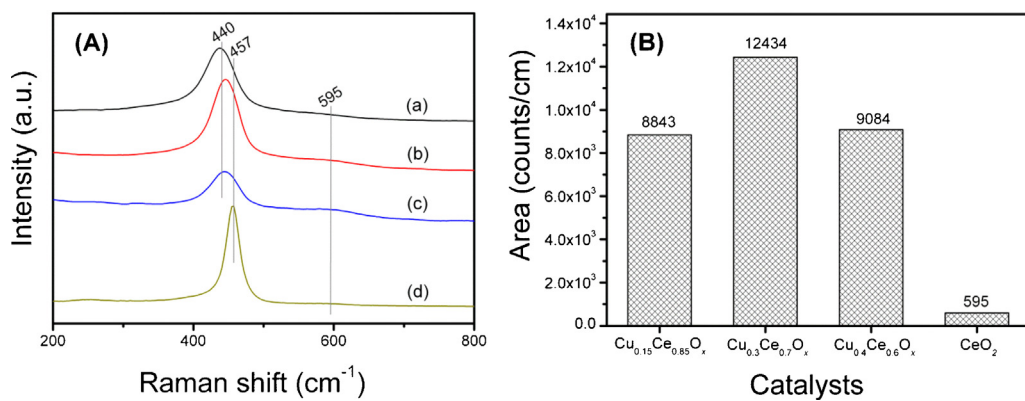


Fig. 10. (A) Raman spectra of (a) $\text{Cu}_{0.15}\text{Ce}_{0.85}\text{O}_x$, (b) $\text{Cu}_{0.3}\text{Ce}_{0.7}\text{O}_x$, (c) $\text{Cu}_{0.4}\text{Ce}_{0.6}\text{O}_x$, and (d) CeO_2 ; (B) integrated peak areas at 595 cm^{-1} for various catalysts.

[39], Cu-Mn/MCM-41 ($T_{90}=320^\circ\text{C}$) [3], 15%CuO-75% $\text{CeO}_2/\gamma\text{-Al}_2\text{O}_3$ ($T_{90}=280^\circ\text{C}$) [6], 6CoO_x/3DOM-ESFO ($T_{90}=270^\circ\text{C}$), and 9.5% MnO_2/HCLT ($T_{90}=292^\circ\text{C}$) [49] are much higher than 220°C . As can be observed, the 1.0%Pt/FS ($T_{90}=200^\circ\text{C}$) [43], 4.9%Au/LaMnO₃ ($T_{90}=225^\circ\text{C}$), 3DOM Co-KIT-6 ($T_{90}=180^\circ\text{C}$) [47], and 0.5%Pd/LaFeO₃ ($T_{90}=221^\circ\text{C}$) [48] also have notable catalytic activities for toluene oxidation, while either the GHSV or toluene inlet concentration is lower than that of the present work. The $\text{Cu}_a\text{Ce}_{1-a}\text{O}_x$ catalysts also possesses superior catalytic performance for propanal oxidation, and 100% propanal conversion are achieved at around 200°C over $\text{Cu}_{0.3}\text{Ce}_{0.7}\text{O}_x$ catalyst. The propanal oxidation efficiency sequence over the synthesized catalysts is basically consistent with that of the toluene oxidation, that is, $\text{Cu}_{0.3}\text{Ce}_{0.7}\text{O}_x \gg \text{Cu}_{0.15}\text{Ce}_{0.85}\text{O}_x > \text{Cu}_{0.4}\text{Ce}_{0.6}\text{O}_x > \text{CuCeO}_x\text{-imp} \gg \text{CuCeO}_x\text{-tcb} > \text{CuO} > \text{CeO}_2$ (see Table 2 and Fig. 12). Above results indicate that the mesoporous $\text{Cu}_a\text{Ce}_{1-a}\text{O}_x$ oxides are potential and powerful catalysts for VOCs low-temperature elimination. The reaction byproducts and CO_2 selectivity (S_{CO_2}) over various catalysts were further investigated, as shown in Fig. 11. It was found that the primary reaction products were CO_2 ($S_{\text{CO}_2} > 99\%$) and H_2O for toluene and propanal oxidation under current conditions, while a little amount (<35 ppm) of benzene can be detected over $\text{CuCeO}_x\text{-tcb}$, CeO_2 , and CuO during toluene combustion. The formation of reaction byproduct benzene can be explained by the combustion mechanism in which the first

step is the cracking the C–C bonds before toluene molecules are completely oxidized to CO_2 and H_2O . No benzene can be detected during the combustion reaction is probably due to the superior activity of the mesoporous $\text{Cu}_a\text{Ce}_{1-a}\text{O}_x$ oxides or the limited benzene produce amount. The Arrhenius plots for the oxidation of toluene and propanal (conversion <15%) are shown in Figs. S2 and S3 [50], and the related reaction rate (r) and apparent activation energy (E_a) were estimated according to the slopes of the Arrhenius plots (see Table 2). It can be observed that the mesoporous $\text{Cu}_a\text{Ce}_{1-a}\text{O}_x$ catalysts possess much higher reaction rates for toluene and propanal oxidation. For example, the reaction rates of $\text{Cu}_{0.3}\text{Ce}_{0.7}\text{O}_x$ (toluene: $r=1.29 \text{ mmol/g h}$ at 220°C ; propanal: $r=4.14 \text{ mmol/g h}$ at 210°C) for toluene and propanal combustion are 1.48–32.25 ($r=0.04\text{--}0.87 \text{ mmol/g h}$) and 1.84–41.4 ($r=0.10\text{--}2.25 \text{ mmol/g h}$) times higher than those of the other catalysts, respectively. In addition, the apparent activation energy values of all $\text{Cu}_a\text{Ce}_{1-a}\text{O}_x$ catalysts are lower than those of the other samples. The above results explain why the $\text{Cu}_a\text{Ce}_{1-a}\text{O}_x$ oxides performed excellently in complete oxidation of toluene and propanal at low-temperatures.

As is known, the input stream to a catalytic oxidation reactor usually contains a mixture of VOCs rather than a single component. In most cases, the mutual effects and oxidation processes are unpredictable due to variable pollutant compositions and catalyst surface properties [51]. Thus, it is important to known whether the

Table 3
Comparison of catalytic performance for toluene destruction over various catalysts.

Catalyst	GHSV (h^{-1})	Concentration (ppm)	T_{90} ($^\circ\text{C}$)	Reference
Mesoporous $\text{Cu}_{0.3}\text{Ce}_{0.7}\text{O}_x$	36,000	1000	212	This work
Mesoporous $\text{Cu}_{0.15}\text{Ce}_{0.85}\text{O}_x$	36,000	1000	231	This work
Cu-Mn/MCM-41	20,000	3500	320	[3]
15%CuO-75% $\text{CeO}_2/\gamma\text{-Al}_2\text{O}_3$	20,000	1000	280	[6]
0.5Cu/NaFAU	10,000	1000	267	[10]
0.5Cu/ZrO ₂	10,000	1000	250	[10]
Ag-Mn/SBA-15	15,000	2500	255	[39]
0.5%Pd/MAC ^a	19,000	1000	370	[40]
0.3%Pd/ZSM-5	26,000	650	270	[41]
FL $\epsilon\text{-MnO}_2$ ^b	20,000	1000	230	[42]
1.0%Pt/FS ^c	33,000	200	200	[43]
4.9%Au/LaMnO ₃	20,000	1000	225	[44]
6CoO _x /3DOM-ESFO ^d	20,000	1000	270	[45]
1.0%Pd/Co ₃ AlO	30,000	800	232	[46]
3DOM Co-KIT-6	20,000	1000	180	[47]
0.5%Pd/LaFeO ₃	15,000	1800	221	[48]
9.5% MnO_2/HCLT ^e	15,000	1000	292	[49]

^a MAC: mesoporous activated carbon.

^b Flower like $\epsilon\text{-MnO}_2$.

^c FS: fibrous silica.

^d 3DOM-ESFO: three-dimensionally ordered macroporous $\text{Eu}_{0.6}\text{Sr}_{0.4}\text{FeO}_3$.

^e HCLT: hydrogen form clinoptilolite zeolite.

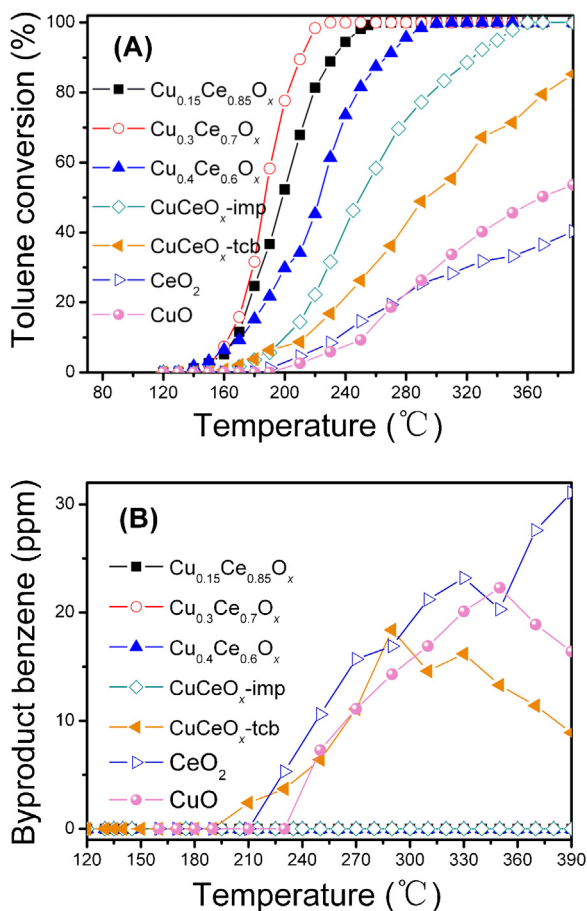


Fig. 11. (A) The light-off curves of toluene oxidation over synthesized catalysts; (B) the reaction byproduct benzene distribution (300 mg catalyst, 1000 ppm toluene, 21% O₂, N₂ balance, GHSV = 36,000

performance of a catalyst with respect to the combustion of a given compound in a mixture is influenced by the presence of other components. In order to address these issues, the catalytic behaviors of co-oxidation of toluene and propanal over $\text{Cu}_{0.3}\text{Ce}_{0.7}\text{O}_x$ catalysts were studied, as displayed in Fig. 13. For comparison purpose, the results obtained from the feed compositions containing the single components are also exhibited in the same figure. Compared with toluene (alone), the oxidation of propanal occurs at significant lower temperature range. When a mixture of toluene and propanal

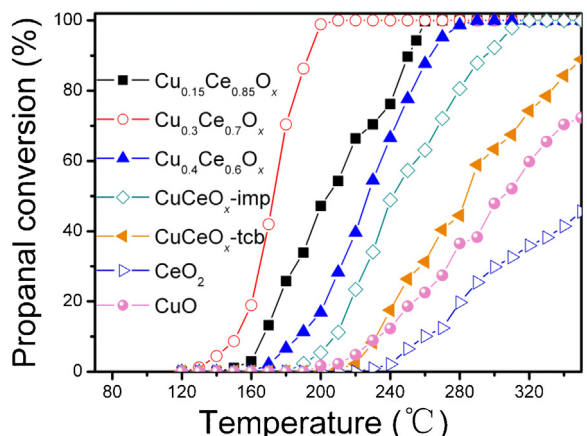


Fig. 12. The light-off curves of propanal oxidation over prepared catalysts (300 mg catalyst, 2500 ppm propanal, 21% O₂, N₂ balance, GHSV = 36,000 h⁻¹).

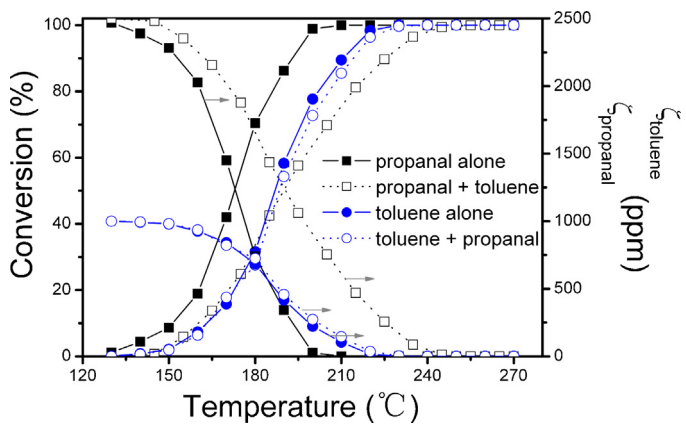


Fig. 13. The co-combustion of toluene and propanal over $\text{Cu}_{0.3}\text{Ce}_{0.7}\text{O}_x$ catalyst (300 mg catalyst, 1000 ppm toluene, 2500 ppm propanal, 21% O₂, N₂ balance, GHSV = 36,000 h⁻¹).

is fed to the reactor, propanal oxidation is remarkably suppressed and its conversion curve is shifted toward higher temperatures by about 20–50 °C, while the toluene oxidation curve is not affected significantly by the presence of propanal (see Fig. 13). This result is much different from that of co-combustion of toluene and propane over 15CuO–75CeO₂ catalyst reported by Saeer et al. (toluene oxidation is obviously inhibited by propane) [6]. As is known, the methyl group in the toluene structure can obviously increase the electronic density of the aromatic ring (that is, the inductive effect), then the interaction between the toluene molecules and the catalyst surface is much stronger than that of propanal molecules with the linear structure [52]. Therefore, the inhibition effect of toluene on propanal oxidation can be attributed to the stronger surface adsorption of toluene molecules.

3.6. Reaction determining factors

It is well accepted that the oxidation of organic compounds over the transition metal oxide catalysts involves a Mars-van Krevelen mechanism, where the organic molecules are primarily oxidized by the lattice oxygen of metal oxides, the latter being re-oxidized by the gas-phase oxygen [10,42,53,54]. The proposed toluene and propanal oxidation reaction pathway is displayed in Fig. 14. A little portion of adsorbed reactant can be oxidized by the oxygen from the support (O_{str}) on account of the excellent oxygen storage capability of CeO₂ and by active adsorbed oxygen from the gas-phase (O_{ad}), and a majority of toluene and propanal molecules are oxidized by the interface lattice oxygen (O_{latt}) release from the CuCeO_x oxides due to the formation of $\text{Cu}_x\text{Ce}_{1-x}\text{O}_{2-\delta}$ solid solution. Researchers proposed that the activation of propane and propene over MnO_x and MnO_x–CeO₂ metal oxides is thought to occur by abstraction of the H atoms from the weakest C–H bonds, with a simultaneous reduction of the surface sites and successive formation of the surface hydroxide ions [25,55]. Herein, it is inferred that the active interface oxygen can also preferentially extract the H atoms from the weakest C–H bonds in the toluene and propanal molecules, and more interface lattice oxygen species should favor the activation of toluene and propanal. The specific surface area, oxygen vacancy, and reducibility of a transition metal oxide are important factors deciding its catalytic activity [10,50,56,57]. In general, the large specific surface area favors the dispersion of active phase, and hence promotes the catalytic process. It can be noticed that the specific surface area of $\text{Cu}_{0.15}\text{Ce}_{0.85}\text{O}_x$ (117.2 m²/g) is obviously lower than that of $\text{Cu}_{0.3}\text{Ce}_{0.7}\text{O}_x$ (139.5 m²/g), while the catalytic performance of the latter is inferior to that of the former one (Table 1 and Figs. 11 and 12). This result indicates that the specific surface area

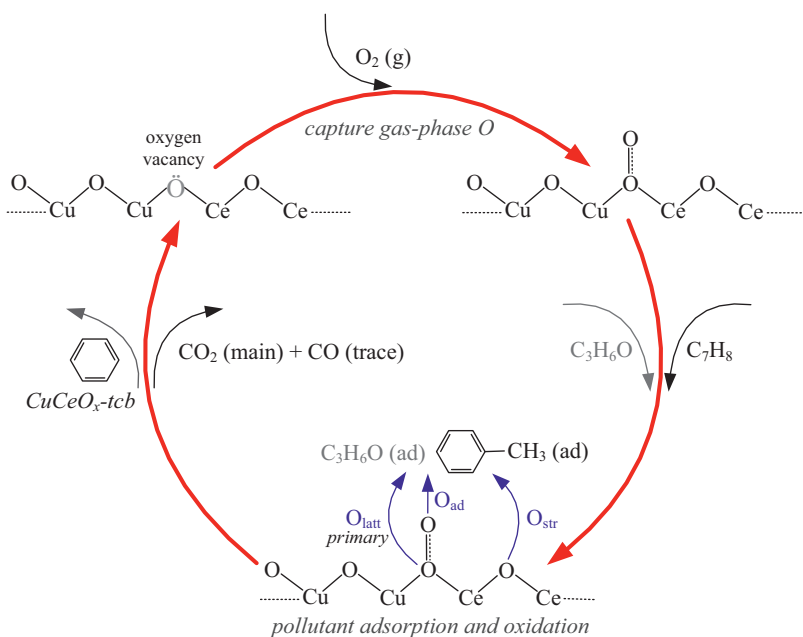


Fig. 14. Proposed toluene and propanal reaction pathway over synthesized CuCeO_x catalysts.

is not the key factor governing the catalytic activity. The presence of oxygen vacancy facilitates the activation of oxygen molecules to active oxygen adspecies, and a good reducibility of the catalysts can provide a facile redox process that would lead to an enhanced catalytic performance [58]. The O 1s XPS and H₂-TPR results reveal that the mesoporous $\text{Cu}_a\text{Ce}_{1-a}\text{O}_x$ catalysts possess higher surface oxygen adspecies concentrations (relevant to the oxygen vacancy density) and better low-temperature reducibility than those of CuCeO_x -imp, CuCeO_x -tcb, CeO_2 , and CuO (Figs. 4 and 8). Moreover, the orders of surface oxygen concentration and reducibility of all synthesized catalysts are in well accordance with the catalytic activity sequence. As a consequence, we conclude that the surface oxygen concentration and low-temperature reducibility are the primary factors determining the catalytic activity during toluene and propanal oxidation.

4. Conclusions

The mesoporous CuO_x - CeO_2 mixed oxide catalysts were successfully synthesized through a simple self-precipitation approach, whose specific surface areas follow a volcano-type manner with the increase of Cu/Ce ratio. The largest specific surface area of *ca.* 162.8 m²/g is achieved on the sample with Cu/Ce atomic ratio of 3/7. Cu species is uniformly dispersed over the mesoporous CuCeO_x samples, and no bulk CuO aggregation can be observed when the Cu content <30 at%. Large portion of Cu²⁺ over mesoporous CuCeO_x catalysts are incorporated into CeO_2 lattice in the form of $\text{Cu}_x\text{Ce}_{1-x}\text{O}_{2-\delta}$ solid solution, leading to structure defects and interface oxygen vacancies. The interaction of Cu and Ce has synergistic effects for the reduction of the mixed oxides. Both the specific surface area and pore diameter are not the key factors governing the catalytic activity. The oxygen adspecies concentration and low-temperature reducibility decrease in the sequence of $\text{Cu}_{0.3}\text{Ce}_{0.7}\text{O}_x > \text{Cu}_{0.15}\text{Ce}_{0.85}\text{O}_x > \text{Cu}_{0.4}\text{Ce}_{0.6}\text{O}_x > \text{CuCeO}_x\text{-imp} > \text{CuCeO}_x\text{-tcb}$, coinciding with the order of their catalytic activities for toluene and propanal oxidation. The mesoporous CuCeO_x catalysts performed much better than their counterparts, and $\text{Cu}_{0.3}\text{Ce}_{0.7}\text{O}_x$ is identified as the most powerful catalysts. For example, the T_{90} temperatures for toluene and propanal oxidation over $\text{Cu}_{0.3}\text{Ce}_{0.7}\text{O}_x$ catalyst have about 110 and 100 °C reduction

comparing with the CuCeO_x -imp sample, respectively. The co-combustion results reveal that toluene can noticeably suppress the oxidation reaction of propanal due to the stronger surface adsorption of toluene molecules. The superior activity of the mesoporous CuCeO_x catalysts can be ascribed to the higher oxygen adspecies concentration and better low-temperature reducibility. We can rationally anticipate that these mesoporous oxides are effective and promising catalysts in the elimination of VOCs, and simultaneously have other potential applications in catalysis, separation and adsorption processes.

Acknowledgements

This work is financially supported by the National Natural Science Foundation (21107106), the Strategic Priority Research Program of the Chinese Academy of Sciences (XDB05050500), the program of Innovation Team of the Bureau of Ningbo Science and Technology (2011B82003), the National Key Technology R&D Program of the Ministry of Science and Technology (2011BAZ01960), the National Basic Research Program of China (2010CB732300), the National High Technology Research and Development Program of China (2012AA063101).

Appendix A. Supplementary data

Supplementary data associated with this article can be found, in the online version, at <http://dx.doi.org/10.1016/j.apcatb.2013.08.039>.

References

- [1] Z. Wang, G.L. Shen, J.Q. Li, H.D. Liu, Q. Wang, Y.F. Chen, *Appl. Catal. B: Environ.* 138–139 (2013) 253–259.
- [2] C. He, F.W. Zhang, L. Yue, X.S. Shang, J.S. Chen, Z.P. Hao, *Appl. Catal. B: Environ.* 111–112 (2012) 46–57.
- [3] W.B. Li, M. Zhuang, T.C. Xiao, M.L.H. Green, *J. Phys. Chem. B* 110 (2006) 21568–21571.
- [4] H.F. Li, G.Z. Lu, Q.G. Dai, Y.Q. Wang, Y. Guo, Y.L. Guo, *Appl. Catal. B: Environ.* 102 (2011) 475–483.
- [5] C. He, J.J. Li, P. Li, J. Cheng, Z.P. Hao, Z.-P. Xu, *Appl. Catal. B: Environ.* 96 (2010) 466–475.
- [6] S.M. Saqer, D.I. Kondarides, X.E. Verykios, *Appl. Catal. B: Environ.* 103 (2011) 275–286.

- [7] D. Delimaris, T. Ioannides, *Appl. Catal. B: Environ.* 89 (2009) 295–302.
- [8] P.M. Heynderickx, J.W. Thybaut, H. Poelman, D. Poelman, G.B. Marin, *J. Catal.* 372 (2010) 109–120.
- [9] X.Y. Wang, Q. Kang, D. Li, *Appl. Catal. B: Environ.* 86 (2009) 166–175.
- [10] M.-F. Luo, J.-M. Ma, J.-Q. Lu, Y.-P. Song, Y.-J. Wang, *J. Catal.* 246 (2007) 52–59.
- [11] J. Papavasiliou, G. Avgouropoulos, T. Ioannides, *Appl. Catal. B: Environ.* 66 (2006) 168–174.
- [12] D. Gamarra, A. Hornés, Zs. Koppány, Z. Schay, G. Munuera, J. Soria, A. Martínez-Arias, *J. Power Sources* 169 (2007) 110–116.
- [13] B. de Rivas, C. Sampedro, M. García-Real, R. López-Fonseca, J.I. Gutiérrez-Ortiz, *Appl. Catal. B: Environ.* 129 (2013) 225–235.
- [14] H.F. Li, G.Z. Lu, Q.G. Dai, Y.Q. Wang, Y. Guo, Y.L. Guo, *ACS Appl. Mater. Interfaces* 2 (2010) 838–846.
- [15] U. Menon, H. Poelman, V. Bliznuk, V.V. Galvita, D. Poelman, G.B. Marin, *J. Catal.* 295 (2012) 91–103.
- [16] Q. Liu, W.-M. Zhang, Z.-M. Cui, B. Zhang, L.-J. Wan, W.-G. Song, *Micropor. Mesopor. Mater.* 100 (2007) 233–240.
- [17] J.L. Cao, Y. Wang, T.Y. Zhang, S.H. Wu, Z.Y. Yuan, *Appl. Catal. B: Environ.* 78 (2008) 120–128.
- [18] J.L. Cao, Y. Wang, X.L. Yu, S.R. Wang, S.H. Wu, Z.Y. Yuan, *Appl. Catal. B: Environ.* 79 (2008) 26–34.
- [19] C.Y. Ma, D.H. Wang, W.J. Xue, B.J. Dou, H.L. Wang, Z.P. Hao, *Environ. Sci. Technol.* 45 (2011) 3628–3634.
- [20] C.Y. Ma, Z. Mu, J.J. Li, Y.G. Jin, J. Cheng, G.Q. Lu, Z.P. Hao, S.Z. Qiao, *J. Am. Chem. Soc.* 132 (2010) 2608–2613.
- [21] G. Avgouropoulos, T. Ioannides, *Appl. Catal. A: Gen.* 244 (2003) 155–167.
- [22] M. Yada, H. Takenaka, M. Machida, T. Kijima, *J. Chem. Soc. Dalton Trans.* 10 (1998), 1547–.
- [23] P. Bera, K.R. Priolkar, P.R. Sarode, M.S. Hegde, S. Emura, R. Kumashiro, N.P. Lalla, *Chem. Mater.* 14 (2002) 3591–3601.
- [24] K.S.W. Sing, D.H. Everett, R.A.W. Haul, L. Moscou, R.A. Pierotti, J. Rouquerol, T. Siemieniewska, *Pure Appl. Chem.* 57 (1985) 603–619.
- [25] Z.-Q. Zou, M. Meng, Y.Q. Zha, *J. Phys. Chem. C* 114 (2010) 468–477.
- [26] Y. Li, Q. Fu, M. Flytzani-Stephanopoulos, *Appl. Catal. B: Environ.* 27 (2000) 179–191.
- [27] S.-M. Zhang, W.-P. Huang, X.-H. Qiu, B.Q. Li, X.-C. Zheng, S.-H. Wu, *Catal. Lett.* 80 (2002) 41–46.
- [28] J. Wang, D. Tsai, T. Huang, *J. Catal.* 208 (2002) 370–380.
- [29] W. Liu, M. Flytzani-Stephanopoulos, *J. Catal.* 153 (1995) 317.
- [30] S. Hočvar, U.O. Krašovec, B. Orel, A.S. Aricó, H. Kim, *Appl. Catal. B: Environ.* 28 (2000) 113–125.
- [31] V.D. Araújo, J.D.A. Bellido, M.I.B. Bernardi, J.M. Assaf, E.M. Assaf, *Int. J. Hydrogen Energy* 37 (2012) 5498–5507.
- [32] L. Qi, Q. Yu, Y. Dai, C.J. Tang, L.J. Liu, H.L. Zhang, F. Gao, L. Dong, *Appl. Catal. B: Environ.* 119–120 (2012) 308–320.
- [33] L.H. Chang, N. Sarirekha, Y.W. Chen, W.J. Wang, *Ind. Eng. Chem. Res.* 45 (2006) 4927–4935.
- [34] R. Zhang, J.T. Miller, C.D. Baertsch, *J. Catal.* 294 (2012) 69–78.
- [35] D. Gamarra, G. Munuera, A.B. Hungría, M. Fernández-García, J.C. Conesa, P.A. Midgley, J.C. Hanson, J.A. Rodríguez, A. Martínez-Arias, *J. Phys. Chem. C* 111 (2007) 11026–11038.
- [36] A. Gurbani, J.L. Ayastuy, M.P. González-Marcos, J.E. Herrero, J.M. Guil, M.A. Gutiérrez-Ortiz, *Int. J. Hydrogen Energy* 34 (2009) 547–553.
- [37] W.J. Shan, Z.C. Feng, Z.L. Li, Z. Jing, W.J. Shen, L. Can, *J. Catal.* 228 (2004) 206–217.
- [38] A. Gurbani, J.L. Ayastuy, M.P. González-Marcos, M.A. Gutiérrez-Ortiz, *Int. J. Hydrogen Energy* 35 (2010) 11582–11590.
- [39] Z.P. Qu, Y.B. Bu, Y. Qin, Y. Wang, Q. Fu, *Appl. Catal. B: Environ.* 132–133 (2013) 353–362.
- [40] J. Bedia, J.M. Rosas, J. Rodríguez-Mirasol, T. Cordero, *Appl. Catal. B: Environ.* 94 (2010) 8–18.
- [41] C. He, J.J. Li, J. Cheng, L.D. Li, P. Li, Z.P. Hao, Z.P. Xu, *Ind. Eng. Chem. Res.* 48 (2009) 6930–6936.
- [42] F.J. Shi, F. Wang, H.X. Dai, J.X. Dai, J.G. Deng, Y.X. Liu, G.M. Bai, K.M. Ji, C.T. Au, *Appl. Catal. A: Gen.* 433 (2012) 206–213.
- [43] J. Uchisawa, K. Kosuge, T. Nanba, S. Masukawa, A. Obuchi, *Catal. Lett.* 133 (2009) 314–320.
- [44] Y.X. Liu, H.X. Dai, J.G. Deng, L. Zhang, B.Z. Gao, Y. Wang, X.W. Li, S.H. Xie, G.S. Guo, *Appl. Catal. B: Environ.* 140–141 (2013) 317–326.
- [45] K.M. Ji, H.X. Dai, J.G. Deng, L.Y. Song, B.Z. Gao, Y. Wang, X.W. Li, *Appl. Catal. B: Environ.* 129 (2013) 539–548.
- [46] P. Li, C. He, J. Cheng, C.Y. Ma, B.J. Dou, Z.P. Hao, *Appl. Catal. B: Environ.* 101 (2011) 570–579.
- [47] Y.S. Xia, H.X. Dai, H.Y. Jiang, L. Zhang, *Catal. Commun.* 11 (2010) 1171–1175.
- [48] J.M. Giraudon, A. Elhachimi, F. Wyrowski, S. Siffert, A. Aboukais, J.-F. Lamonié, G. Leclercq, *Appl. Catal. B: Environ.* 75 (2007) 157–166.
- [49] G.S.P. Soylu, Z. Özçelik, İ. Boz, *Chem. Eng. J.* 162 (2010) 380–387.
- [50] C.Y. Chen, J. Zhu, F. Chen, X.J. Meng, X.M. Zheng, X.H. Gao, F.-S. Xiao, *Appl. Catal. B: Environ.* 140–141 (2013) 199–205.
- [51] C. He, P. Li, J. Cheng, Z.-P. Hao, Z.-P. Xu, *Water Air Soil Pollut.* 209 (2010) 365–376.
- [52] S. Ordóñez, L. Bell, H. Sastre, R. Rosal, F.V. Díez, *Appl. Catal. B: Environ.* 38 (2002) 139–149.
- [53] R.H. Wang, J.H. Li, *Environ. Sci. Technol.* 44 (2010) 4282–4287.
- [54] V.P. Santos, M.F.R. Pereira, J.J.M. Órfão, J.L. Figueiredo, *Appl. Catal. B: Environ.* 99 (2010) 353–363.
- [55] M. Baldi, V.S. Escribano, J.M.G. Amores, F. Milella, G. Busca, *Appl. Catal. B: Environ.* 17 (1998) L175–L182.
- [56] C. He, Q. Li, P. Li, Y.F. Wang, X.Y. Zhang, Z.P. Hao, *Chem. Eng. J.* 162 (2010) 901–909.
- [57] S.C. Kim, W.G. Shim, *Appl. Catal. B: Environ.* 98 (2010) 180–185.
- [58] J.Q. Torres, J.-M. Giraudon, J.-F. Lamonié, *Catal. Today* 176 (2011) 277–280.